We are IntechOpen, the world's leading publisher of Open Access books
Built by scientists, for scientists

4,800
Open access books available

122,000
International authors and editors

135M
Downloads

Our authors are among the

154
Countries delivered to

TOP 1%
most cited scientists

12.2%
Contributors from top 500 universities

WEB OF SCIENCE™

Selection of our books indexed in the Book Citation Index in Web of Science™ Core Collection (BKCI)

Interested in publishing with us?
Contact book.department@intechopen.com

Numbers displayed above are based on latest data collected.
For more information visit www.intechopen.com

Chapter 12

Surface Characterization by the Use of Digital Holography

Dahi Ghareab Abdelsalam, Takeshi Yasui,
Takayuki Ogawa and Baoli Yao

Additional information is available at the end of the chapter

http://dx.doi.org/10.5772/66082

Abstract

Digital holography (DH) is an attractive measuring optical technique in the fields of engineering and science due to its remarkable accuracy and efficiency. The holograms are recorded by an interferometer and reconstructed by numerical methods such as Fresnel transform, convolution approach, and angular spectrum. Because harmful coherent noise often arises when long coherent lengths are used, bright femtosecond pulse light with ultrashort coherent length may be the solution to reduce both spurious and speckle noises. Since the usual DH uses a visible light, it is difficult to visualize 3D internal structure of visibly opaque objects due to their limited penetration depth. The terahertz (THz) radiation has a good penetration capability; thus, 3D visualization of both surface shape and internal structure in visibly opaque object can be achieved via THz-DH technique.

Keywords: digital holography, numerical reconstruction, 3D surface metrology, femtosecond DH, terahertz DH

1. Introduction

Various optical techniques have been developed for measuring 3D shape from a single position. The height distribution of the surface of the object is encoded into a deformed fringe pattern, and then shape is directly decoded by one of those optical techniques. DH is considered one of those optical techniques that have received much interest for surface characterization. DH has been heavily developed over recent years because of newly available high-resolution charge-coupled device (CCD) cameras and advances in digital and automated image processing techniques. Performing Fourier transforms and spectral filtering without the need for additional optical

INTECH
open science | open minds

© 2017 The Author(s). Licensee InTech. This chapter is distributed under the terms of the Creative Commons Attribution License (http://creativecommons.org/licenses/by/3.0), which permits unrestricted use, distribution, and reproduction in any medium, provided the original work is properly cited. CC BY

components for reconstruction has given advantages of digital holography over conventional optical holography. DH enables the extraction of both amplitude and phase information of objects in real time with high resolution. DH technique is less sensitive to external perturbations and has long-term stability in object measurement. DH has merits of wide applications covering particles, living cells, and 3D profiling and tracking of micro-objects or nano-objects. In this chapter, we present recent developments in DH techniques carried out by the author. In Section **2**, the principle of holography with highlights on three numerical reconstruction methods, namely, Fresnel approximation, convolution approach, and angular spectrum, is explained. In Section **3**, the impact of slightly imperfect collimation of the reference wave in off-axis DH is presented. In Section **4**, low-coherence, off-axis digital holographic microscope (DHM) by the use of femtosecond pulse light for measuring fine structure of in vitro sliced sandwiched biological sarcomere sample is described. In Section **5**, off-axis terahertz DH using continuous-wave radiation generated from cascade laser source for testing a letter T from paper is described. Section **6** gives concluding discussions and remarks.

2. The principle of holography

The word holography is derived from the Greek words "holos," which means whole or entire, and graphein, which means to write. Holography is a method that records and reconstructs both irradiance of each point in an image and the direction in which the wave is propagating at that point. Holography consists of two procedures: recording as shown in **Figure 1(a)** and reconstruction as shown in **Figure 1(b)**. Because of the development of digital recording process for recording and computer technology for numerical reconstruction, the optical

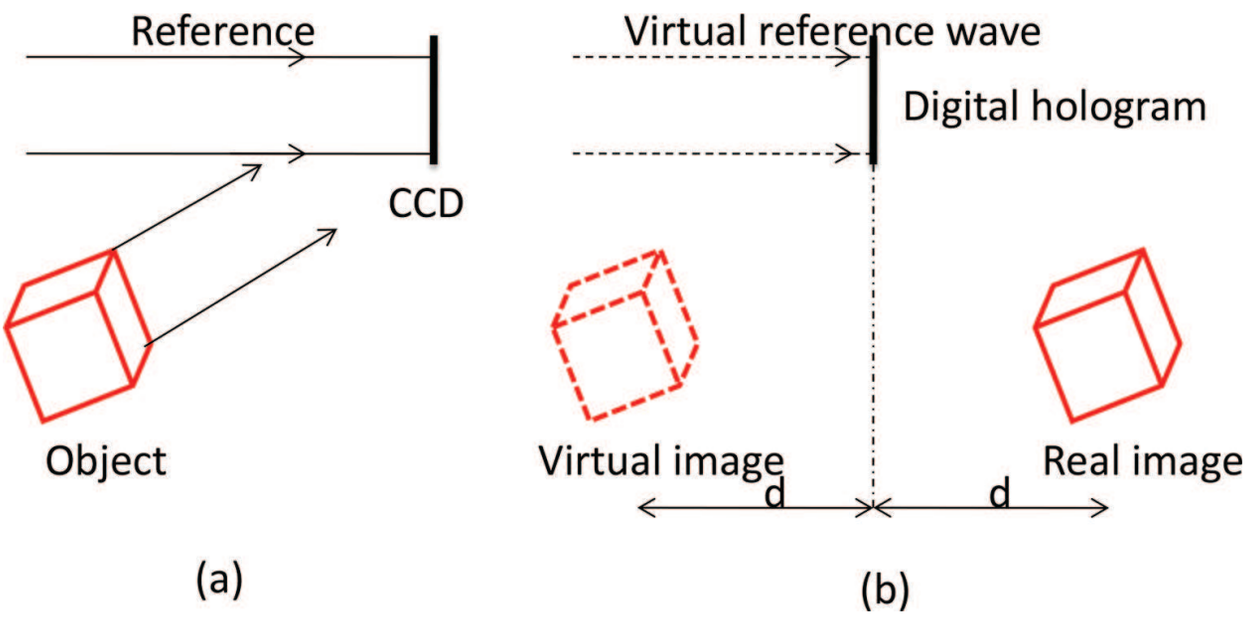

Figure 1. Principle of digital holography: (a) recording and (b) reconstruction with reference wave.

http://dx.doi.org/10.5772/66082

holography has been replaced by digital holography. The idea of numerical reconstruction was proposed by Goodman and Lawrence [1]. In 1993, Schnars and Juptner [2] used a CCD camera to record a hologram and performed numerical reconstruction in order to reconstruct this digital hologram.

2.1. Numerical reconstruction in digital holography

In digital holography, the CCD or Complementary Metal-Oxide Semiconductor (CMOS) camera captures the image and transfers it to the computer. This image is saved digitally as a digital hologram. This hologram is digitally accessed and numerically reconstructed by a virtual reference wave, which effectively simulates the reference wave used in the process of recording. The speed of reconstruction procedure depends on the implementation of the numerical reconstruction algorithm and the speed of the computer processing. Because the reference wave has to be generated virtually in the computer, a plane wave or a spherical wave is usually used in the recording process. **Figure 1** shows the typical setup of digital holography and the reconstruction with virtual reference wave. Let us consider the coordinate system as shown in **Figure 2**; then the diffraction by the aperture or hologram in the distance of d along the propagation direction of the wave can be quantitatively described by Fresnel-Kirchhoff integral [3].

If the reference wave is set up to be nominally normal incident to the hologram, then the diffracted light is approximated by the Fresnel-Kirchhoff integral as

$$\Gamma\left(\eta',\xi'\right)=\frac{i}{\lambda}\int_{-\infty}^{-\infty}\int_{-\infty}^{-\infty}U_h(x,y)U_r(x,y)\frac{\exp\left(-i\frac{2\pi}{\lambda}\rho'\right)}{\rho'}dxdy \tag{1}$$

where $\Gamma(\eta', \xi')$ is the diffraction pattern, $U_h(x, y)$ is the digital hologram captured by the CCD camera, λ is the wavelength of the light in the virtual reference beam used in the reconstruction, ρ' is the distance between a point in the hologram plane and a point in the reconstruction plane, which has the form $\rho'=\sqrt{\left(x-\xi'\right)^2+\left(y-\eta'\right)^2+d^2}$, and $U_r(x, y)$ is the function describing the reference wave. In Eq. (1), $\Gamma(\eta', \xi')$ is the diffraction pattern calculated at a distance d behind the CCD plane (see **Figure 2**), which means it reconstructs the complex amplitude in the plane of the real image. Therefore, both the intensity and the

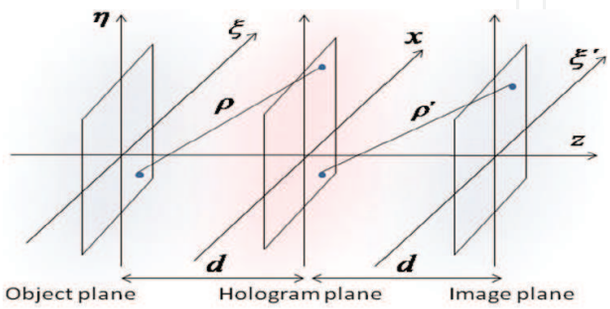

Figure 2. Coordinate system for numerical hologram reconstruction.

phase information can be obtained after numerical reconstruction. The reconstructed intensity is written as

$$I(\eta', \xi') = \left|\Gamma(\eta', \xi')\right|^2 \tag{2}$$

And the reconstructed phase is

$$\varphi(\eta', \xi') = \arctan\frac{\mathrm{Im}\left[\Gamma(\eta', \xi')\right]}{\mathrm{Re}\left[\Gamma(\eta', \xi')\right]} \tag{3}$$

where Re denotes the real part and Im denotes the imaginary part. The calculated diffraction pattern is the complex amplitude at a distance d behind the CCD plane where the real image is reconstructed. However, the real image could be distorted by the reference wave. To avoid this effect and ensure that an undistorted real image is left, a conjugate reference wave has to be introduced in the reconstruction. Then the calculated diffraction pattern is rewritten as

$$\Gamma(\eta, \xi) = \frac{i}{\lambda}\int_{-\infty}^{-\infty}\int_{-\infty}^{-\infty} U_h(x, y)U_r^*(x, y)\frac{\exp\left(-i\frac{2\pi}{\lambda}\rho\right)}{\rho}dxdy \tag{4}$$

with

$$\rho = \sqrt{(x-\xi)^2 + (y-\eta)^2 + d^2} \tag{5}$$

where $U_r^*(xy)$ is conjugate to the original reference wave $U_r(x, y)$. Both results from Eq. (1) and Eq. (4) are equivalent because $U_r(xy) = U_r^*(xy)$. As illustrated above, Eq. (4) is the key formula of digital holography, and it is essential to calculate it numerically to perform numerical reconstruction of a digital hologram. The direct approach of Eq. (4) is not feasible in terms of the calculation complexity and computer run time. Some approximations have to be applied in order to calculate the double integral to make the numerical reconstruction effective and efficient. According to the approximation used in the algorithm, the numerical reconstruction can be classified into three types: Fresnel approximation, convolution approaches, and angular spectrum.

2.1.1. Reconstruction by the Fresnel approximation

In digital holography, the values of the coordinates x and y as well as ξ and η are very small compared to the distance d between the reconstruction plane and the CCD or CMOS device. If now the right hand side of Eq. (5) is expanded to a Taylor series and the fourth term is smaller than the wavelength,

$$\frac{\left[(x-\xi)^2 + (y-\eta)^2\right]^2}{8d^3} << \lambda \tag{6}$$

http://dx.doi.org/10.5772/66082

the effect of it and the terms after it are negligible, and they can be removed. Thus the distance ρ can be approximated as

$$\rho = d + \frac{(\xi - x)^2}{2d} + \frac{(\eta - y)^2}{2d} \tag{7}$$

Replacing the denominator in Eq. (4) with d and inserting Eq. (7) into it, the following expression results in the reconstruction of the real image:

$$\begin{aligned} \Gamma(\eta,\xi) &= \frac{i}{\lambda d}\exp\left(-i\frac{2\pi}{\lambda}d\right)\exp\left(-i\frac{\pi}{\lambda d}\left(\xi^2+\eta^2\right)\right) \\ &\times \int_{-\infty}^{-\infty}\int_{-\infty}^{-\infty} U_r^*(x,y)U_h(x,y)\exp\left(-i\frac{\pi}{\lambda d}\left(x^2+y^2\right)\right)\exp\left(-i\frac{2\pi}{\lambda d}(x\xi+y\eta)\right)dxdy \end{aligned} \tag{8}$$

This equation is known as the Fresnel approximation or Fresnel transformation due to its mathematical similarity with the Fourier transform.

The intensity is calculated by squaring

$$I(\eta,\xi) = |\Gamma(\eta,\xi)|^2 \tag{9}$$

And the phase is calculated by

$$\varphi(\eta,\xi) = \arctan\frac{\mathrm{Im}[\Gamma(\eta,\xi)]}{\mathrm{Re}[\Gamma(\eta,\xi)]} \tag{10}$$

To convert the discrete Fresnel transformation in Eq. (8) to a digital implementation, two substitutions are applied [4]:

$$\nu = \frac{\xi}{\lambda d}; \quad \mu = \frac{\eta}{\lambda d}; \tag{11}$$

Therefore Eq. (8) turns into

$$\begin{aligned} \Gamma(\nu,\mu) &= \frac{i}{\lambda d}\exp\left(-i\frac{2\pi}{\lambda}d\right)\exp\left(-i\pi\lambda d\left(\nu^2+\mu^2\right)\right) \\ &\times \mathfrak{F}^{-1}\left\{U_r^*(x,y)U_h(x,y)\exp\left(-i\frac{\pi}{\lambda d}\left(x^2+y^2\right)\right)\right\} \end{aligned} \tag{12}$$

Because the maximum frequency is determined by the sampling interval in the spatial domain according to the theory of the Fourier transform, the relationships among Δx, Δy, $\Delta \nu$, and $\Delta \mu$ are

$$\Delta\nu = \frac{1}{N\Delta x}; \quad \Delta\mu = \frac{1}{N\Delta y} \tag{13}$$

With Eq. (13), Eq. (12) can be rewritten as

$$\Gamma(m,n) = \frac{i}{\lambda d}\exp\left(-i\frac{2\pi}{\lambda}d\right)\exp\left(-i\pi\lambda d\left(\frac{m^2}{N^2\Delta x^2}+\frac{n^2}{N^2\Delta y^2}\right)\right) \times \mathfrak{F}^{-1}\left\{U_r^*(k,l)U_h(k,l)\exp\left(-i\frac{\pi}{\lambda d}\left(k^2\Delta x^2+l^2\Delta y^2\right)\right)\right\} \tag{14}$$

Eq. (14) is known as the discrete Fresnel transform. The matrix Γ is calculated by applying an inverse discrete Fourier transform to the product of $U_r^*(k,l)$ with $U_h(k,\ l)$ and $\exp(-i\pi(k^2\Delta x^2 + l^2\Delta y^2)/(\lambda d))$. The calculation can be done very effectively using the fast Fourier transform (FFT) algorithm.

2.1.2. Reconstruction by the convolution approach

This method makes use of the convolution theorem. This approach was introduced to digital holography by Kreis and Juptner [5]. Eq. (4) can be interpreted as a superposition integral:

$$\Gamma(\eta,\xi) = \int_{-\infty}^{-\infty}\int_{-\infty}^{-\infty} U_h(x,y)U_r^*(x,y)g(\eta,\xi,x,y)dxdy \tag{15}$$

where the impulse response $g(\eta, \xi, x, y)$ is given by

$$g(\eta,\xi,x,y) = \frac{i}{\lambda}\frac{\exp\left[-i\frac{2\pi}{\lambda}\rho\right]}{\rho} \tag{16}$$

Eq. (15) can be regarded as a convolution and the convolution theorem can be applied. The convolution theorem states that the Fourier transform of the convolution of two functions is equal to the product of the Fourier transforms of the individual functions. In other words, the convolution of two functions in the spatial domain can be easily obtained through the multiplication of them in another domain, namely, spatial frequency domain.

Applying the convolution theorem to Eq. (**4**), it is converted to

$$\Gamma(\eta,\xi) = \mathfrak{F}^{-1}\left\{\mathfrak{F}\left(U_h(x,y).U_r^*(x,y)\right).\mathfrak{F}(g(x,y))\right\} \tag{17}$$

Eq. (17) includes two forward Fourier transformations and one inverse Fourier transformation, all of which can be practically implemented via the FFT algorithm. Both Fresnel and convolution methods are practically implemented via the FFT algorithm. In the Fresnel approximation, only a forward FFT is performed. However, two or three FFTs are performed in the convolution approach. In the convolution approach, the pixel sizes in the reconstructed image are equal to that of the hologram. It would seem that a higher resolution could be achieved if a CCD or CMOS device with a smaller pixel size was used in the recording process. For applications that detect very small objects, the convolution approach has more advantages and is more accurate than the Fresnel approximation algorithm.

http://dx.doi.org/10.5772/66082

2.1.3. Reconstruction by the angular spectrum method

Both the Fresnel approximation and the convolution approach suffer the same limitation, i.e., that the object under observation must be placed farther away than some minimum distance. If it is placed inside this distance, the spatial frequency of the detector is too low and aliasing occurs. This minimum distance is given [6]:

$$d_{\min} = \frac{(N\Delta x)^2}{N\lambda} \tag{18}$$

where N and Δx are the number and the size of the pixels. However, the angular spectrum method [7] is able to overcome this disadvantage. It is comparable with the other methods in terms of computational efficiency but has the potential of higher accuracy. If the wave field at the plane $d = 0$ is $U_0(x,y;0)$, the angular spectrum $A(k_x,k_y;0)$ at this plane is obtained by taking the Fourier transform:

$$A(k_x, k_y; 0) = \int\int U_0(x, y; 0)\exp\{-i(k_x x + k_y y)\}dxdy \tag{19}$$

where k_x and k_y are the corresponding spatial frequencies of x and y. The angular spectrum at the distance d, i.e., $A(k_x,k_y;d)$, is calculated from $A(k_x,k_y;0)$ as given by

$$A(k_x, k_y; d) = A(k_x, k_y; 0)\exp(ik_z d) \tag{20}$$

where $k_z = \sqrt{k^2 - k_x^2 - k_y^2}$. The reconstructed complex wave field at any plane perpendicular to the propagating z axis is found by

$$U(\xi, \eta; d) = \int\int A(k_x, k_y; d)\exp\left[i(k_x\xi + k_y\eta)\right]dk_x dk_y = \mathfrak{F}^{-1}\left[\mathfrak{F}(U_0)\exp(ik_z d)\right] \tag{21}$$

The resolution of the reconstructed images from the angular spectrum method is the same as that in the hologram plane, which means that the pixel size does not vary with changes of wavelength or reconstruction distance.

3. Impact of imperfect collimation of the reference wave in off-axis DH

In digital holography, the simulation of the plane wave is essential for performing a numerical reconstruction. Conventionally, a shear interferometer is used for producing perfect collimation and hence producing a perfect plane wave. In Section 3, we show that using a slightly imperfect plane wave in digital holography experiments is acceptable [8]. We experimentally proved that by using the Mickelson interferometer, no influence of imperfect collimation of the reference wave in an off-axis digital holography exists, as has been previously claimed. We applied perfect and imperfect collimations to three different surface (flat, spherical, and step height) shapes for height inspection, and the results were almost in good agreement. The samples being tested were mounted in the Michelson interferometer one by one, as shown in

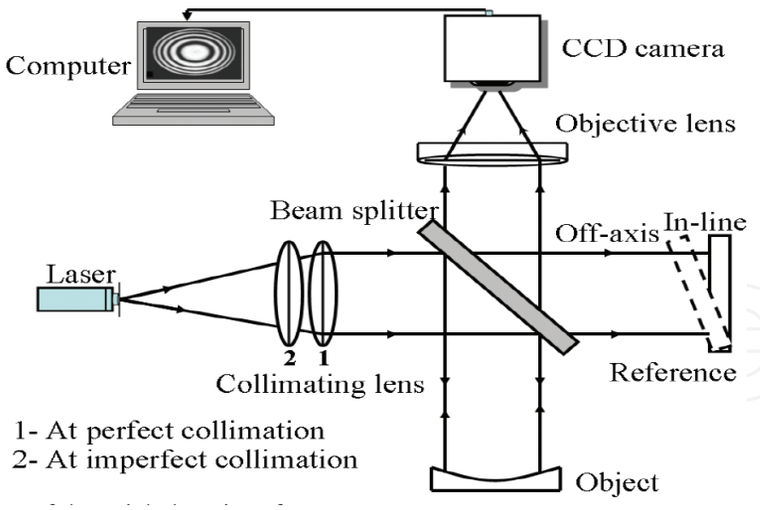

Figure 3. Schematic diagram of the Michelson interferometer.

Figure 3. A laser diode beam passed through a collimating lens of focal lens 100 mm and expanded. The beam splitter splits the collimated beam into two equal beams: one for reference (optical flat of $\lambda/20$ flatness) arm and the other for the object (flat, spherical, and step height surfaces) arm. The beam reflected from the reference and the object is recombined at the beam splitter to produce an interference pattern. The perfect collimation that produced a perfect plane wave impinging on the reference was adjusted by a shear interferometer placed between the collimating lens and the beam splitter.

The slightly imperfect collimations were seven equidistance displacements of the collimating lens with 1.5 mm from the perfect collimation and between two successive displacements. The off-axis holograms for the samples under test at perfect and slightly imperfect plane waves were captured and then reconstructed. Details of the reconstruction process are explained in reference [8]. The reconstructed phase for perfect **Figure 4(a)** and slightly imperfect collimations **Figure 4(2–8)** and the height line profile for both along the central x-axis are shown in **Figure 4(1(b)–1(c))**, respectively.

The wrapping phase for the spherical surface for perfect collimations and slightly imperfect collimations is shown in **Figure 5(a)** and **(2–8)**, respectively. The unwrapping phases of **Figure 5b**(**1–8**) are shown in **Figure 5c(1–8)**, and the height line profiles along the central x-axis of **Figure 5b**(**1–8**) are shown in **Figure 5d**(**1–8**), respectively.

For the third object (step height surface), the off-axis holograms at the perfect and slightly imperfect collimations were captured and reconstructed. The height line profiles along the central x-axis of the reconstructed heights at perfect and slightly imperfect collimations at imaging and Fresnel transform are shown in **Figure 6a** and **b**, respectively.

As seen from **Figures 4**–**6**, for flat, spherical, and step surfaces, the measured height values of the three tested surfaces were almost consistent at perfect and imperfect collimations. Very small variations may be observed due to noise, which is commonly observed in interferometry measurements. We claim that the variations may be due to the mechanical imperfection of the collimating lens as shown in **Figure 7**. We claim that when the lens mounting was ideally

http://dx.doi.org/10.5772/66082

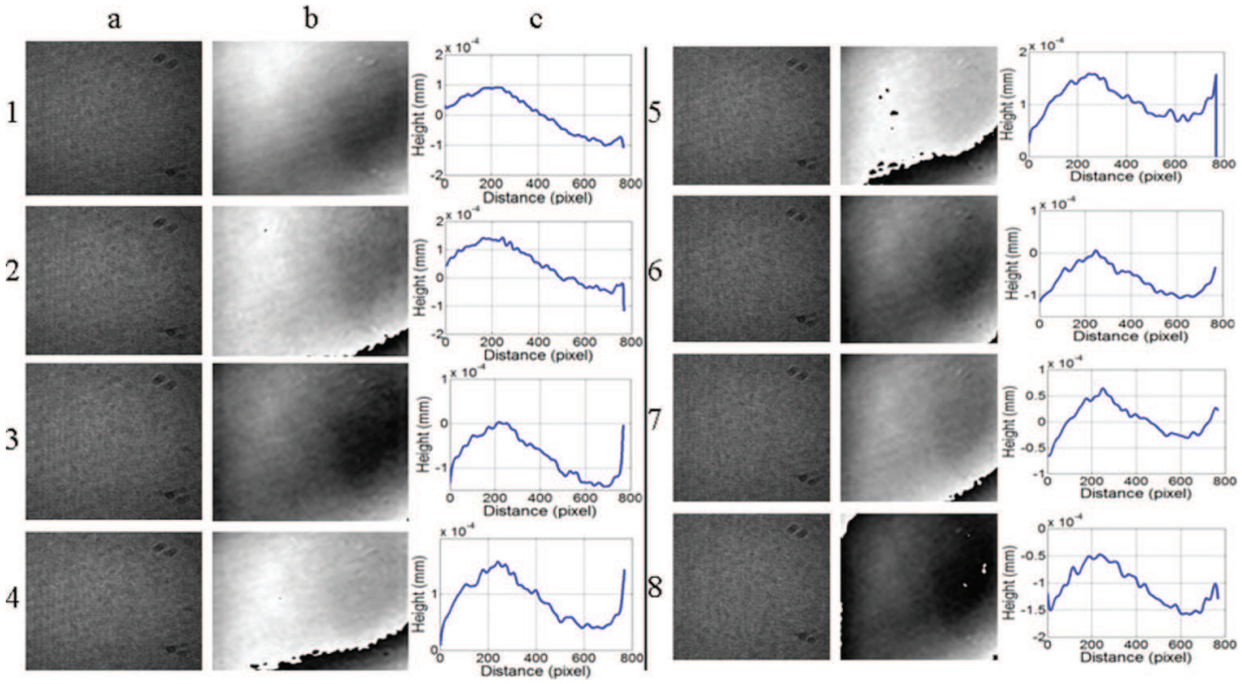

Figure 4. (a) Off-axis interferograms. (b) Reconstructed phases of (a). (c) Line height profiles along the central *x*-axis of the tested flat surface produced at (1) perfect collimation and (2–8) slightly imperfect collimations.

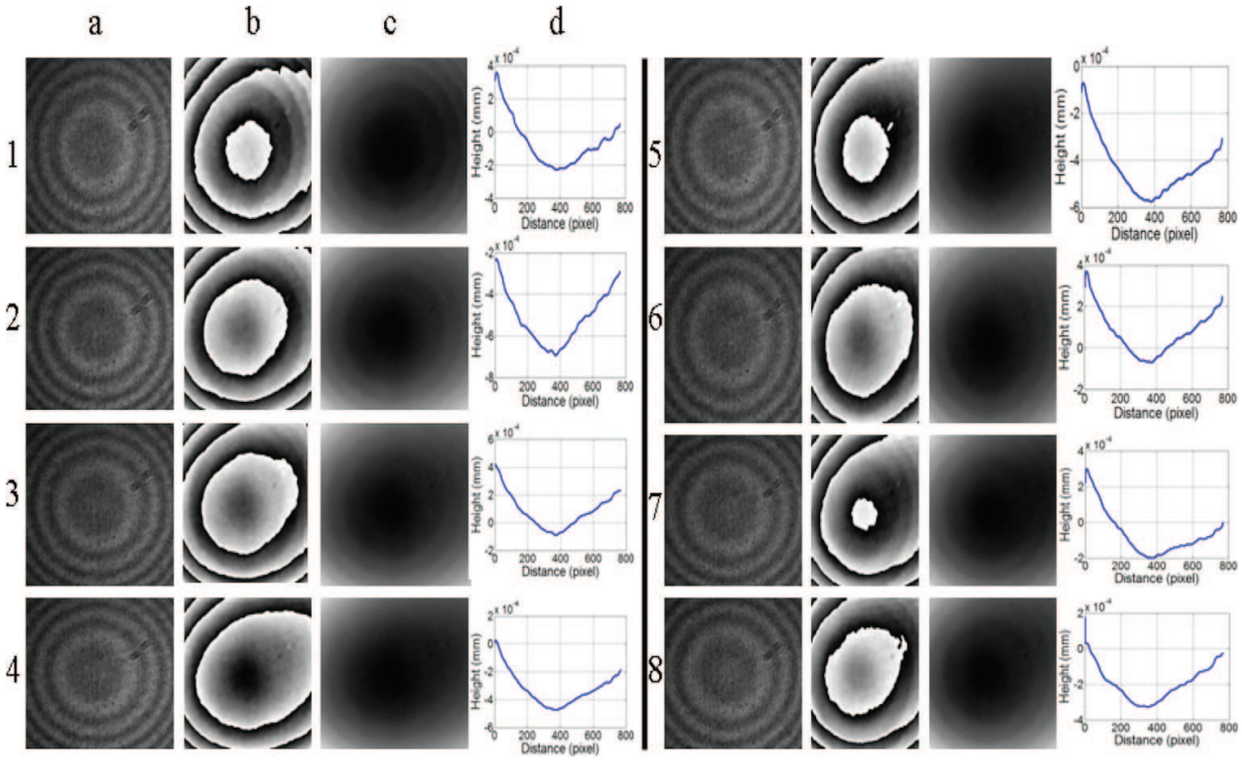

Figure 5. (a) Off-axis interferograms. (b) Reconstructed phases of (a). (c) Unwrapping phases of (b). (d) Line height profiles along the central *x*-axis of the tested spherical surface produced at (1) perfect collimation and (2–8) imperfect collimations.

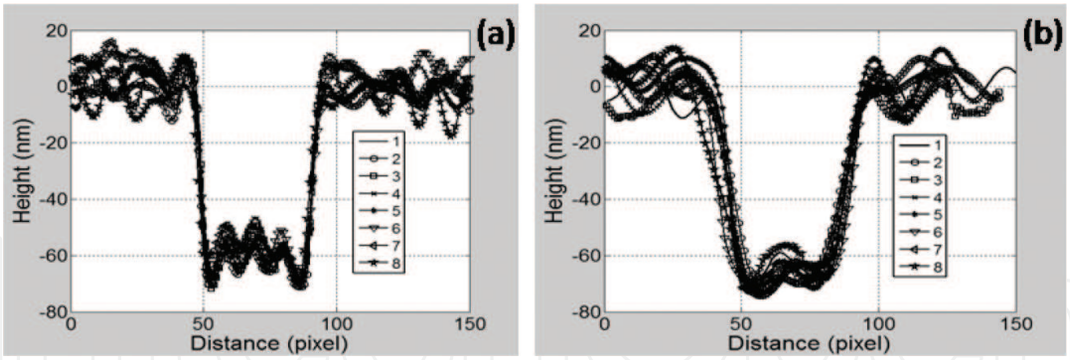

Figure 6. Line height profiles of the tested step surface at perfect (1) and imperfect (2–8) collimations produced at (a) $d = 0.0$ mm (imaging scheme) and (b) $d = -500.0$ mm (Fresnel transform).

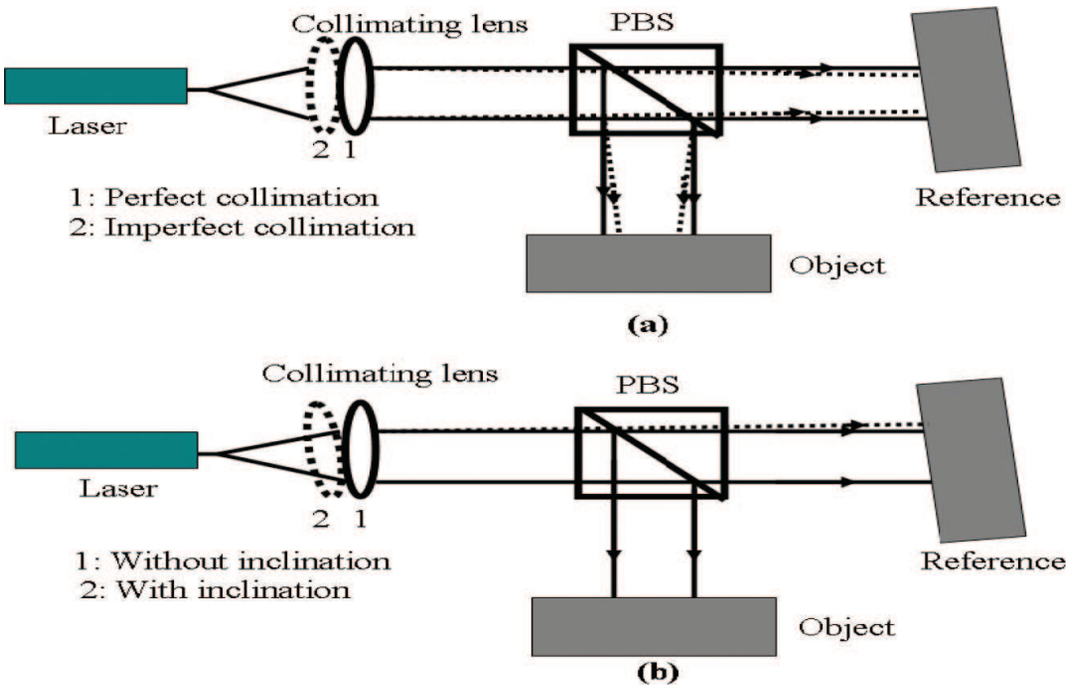

Figure 7. The effect of design of mounting and the adjustment of the collimation lens on the very small height variations: (a) ideal mounting, (b) nonideal mounting.

displaced as shown in **Figure 7(a)** at position 2 (slightly imperfect collimation), the beams converge toward the reference and the object. The convergent beams would then be canceled out and subsequently have no impact on the height variations. However, it is hard to achieve ideal mounting mechanically. Thus we expect that the effect of nonideal mounting as shown in **Figure 7(b)** may be the reason of small height variations as shown in **Figure 7(b)**.

4. Low coherence, off-axis DHM for in vitro sandwiched biological samples investigation

In digital holographic microscopy (DHM), optical sources with long coherent lengths such as He-Ne laser have been widely used to feature the sample. Because of the high degree of

coherence of the He-Ne laser light, harmful coherent noise often arises. This noise affects the quality of the holograms and hence leads to error in phase measurement. The larger the phase noise is, the lower the measurement precision will be. The harmful coherent noise is mainly classified into two types. The first is the random diffraction patterns (speckle noise) due to scattered light. The second is the formation of unwanted interference fringes (spurious noise) due to stray light. The spurious noise is formed when light reflected or scattered from various surfaces in the optical path is coherent with the main beam. The amplitude of the scattered light a_s adds vectorially to the amplitude of the main beam, resulting in a phase error $\Delta\phi$ as illustrated in **Figure 8(a)**. Some practical solutions such as introducing a wedged beam splitter, a rotating diffuser, and antireflection coating to the optical surfaces, in the optical system setup, were proposed to minimize the unwanted coherent noise. Although these practical solutions are effective and may circumvent to suppress the coherent noise to some amount, they have some drawbacks in terms of blurring the fringe visibility and hindering the fringe formation in DHM, which require perfect alignment. Optical sources with short coherent lengths such as LEDs were proposed in order to avoid the harmful coherent noise. However, the limited coherence length of LED and its insufficient brightness hinder its application in an off-axis DHM, since just a limited number of interference fringes with poor visibility appear in the field of view (FOV). In Section 4, we present an off-axis DHM configuration using bright femtosecond pulse light with ultrashort coherent length, which makes possible to feature sandwiched biological samples with no coherent noise (speckle and spurious) in the reconstructed object wave [9].

A typical configuration of the sandwiched biological sample is shown in **Figure 8(b)**, where the specimen is mounted in between two thin glass plates to avoid dehydration. Investigating such biological samples using conventional DHM with long coherent He-Ne laser light is challenging because of existence of the harmful coherent noise. Photograph of the investigated sample taken by the proposed DHM system (see **Figure 9**) with blocking the reference arm is shown in **Figure 8(c)**. The DHM experimental setup is schematically shown in **Figure 9**. The configuration is comprised of two parts: generation of femtosecond pulse light in near-infrared region and a Mach-Zehnder interferometer in transmission. A mode-locked Er-doped fiber laser light (center wavelength λ_c = 1550 nm, spectral bandwidth $\Delta\lambda$ = 73 nm, pulse duration $\Delta\tau$ = 100 fs, mean power P_{mean} = 380 mW, and repetition frequency f_{rep} = 250 MHz) was focused on a periodically poled lithium niobate (PPLN) crystal to convert the wavelength by second

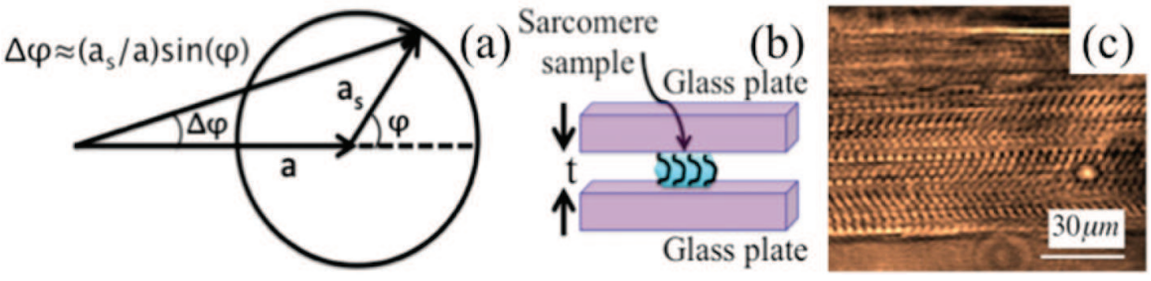

Figure 8. (a) Phase error $\Delta\phi$ produced by scattered long coherent light $\mathbf{a}_s$, (b) sliced biological specimen mounted in between two thin glass plates to avoid dehydration, and (c) photograph of the investigated sarcomere sample taken by the proposed setup with blocking the reference arm.

harmonic generation (SHG) into the operating wavelength region of a charge-coupled device (CCD) camera used. To extract the SHG light, we used a narrow band-pass optical filter (F, passband wavelength = 775 ± 5 nm). The extracted SHG light has λ_c of 777.8 nm, $\Delta\lambda$ of 10 nm, $\Delta\tau$ of 120 fs, and P_{mean} of 14 mW (left inset of **Figure 9**).

The output power was sufficient to illuminate the sample and produce off-axis holograms with high contrast in the entire field of the CCD camera. The coherence length of the SHG pulse light was 30 μm. The SHG beam was expanded to a diameter of 20 mm by a telescope system. In the Mach-Zehnder off-axis setup in transmission, a pair of non-polarized beam splitters (NPBS1 and NPBS2) was used to separate the two SHG beams into reference (*R*) and object (*O*) beams and combine them again. Difference of optical path length in the two arms was precisely adjusted within the coherence length of 30 μm by a scanning mirror, equipped with a mechanical translation stage, in the reference arm. The interfering object beam and the reference beam were tilted at small angle with respect to each other to produce off-axis hologram at the plane of the beam splitter NPBS2. The off-axis hologram was transferred via a microscope lens MO3 (20 × , NA = 0.1) to a black-and-white CCD camera (640 pixels by 480 pixels, pixel size = 4.3 μm). We conducted the experiment on microstructured sarcomere sample, which was isolated fibers dissected from rabbit muscle and mounted in between two thin glass plates to avoid dehydration (gap distance t = 15 μm) as shown in **Figure 8(c)**. The off-axis hologram was recorded by making the reference wave (instead of the object wave) subtending the off-axis angle with the optical axis. Such arrangement is not only easier to align but also makes the image plane parallel to the sensor surface.

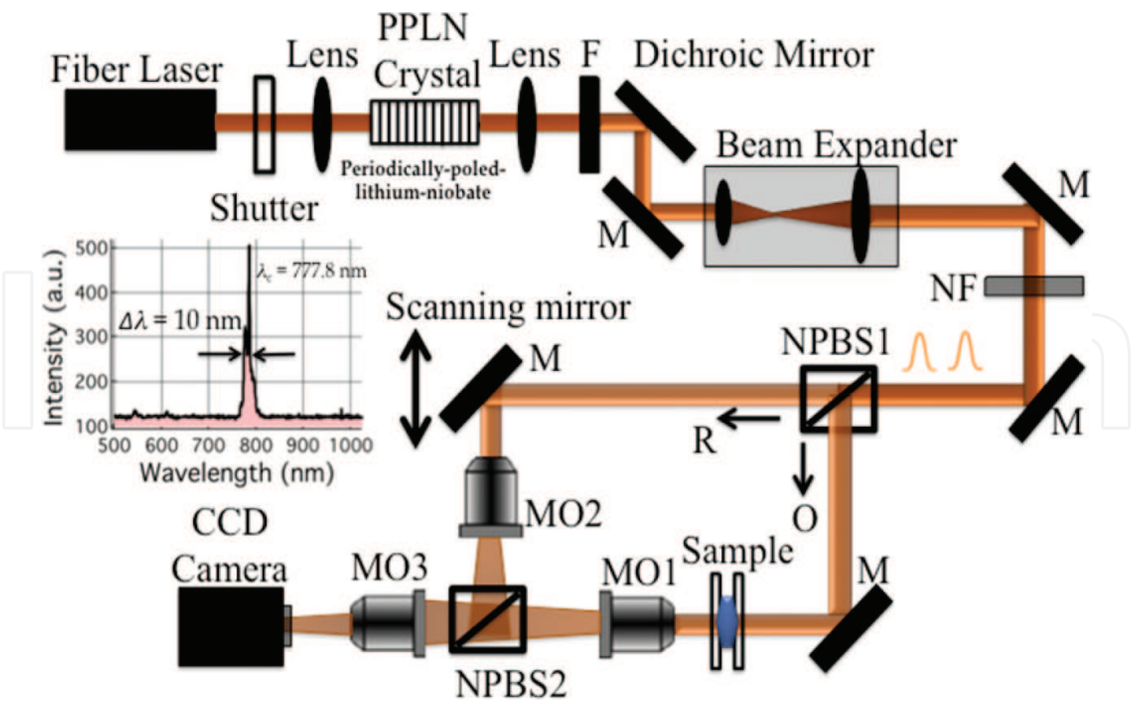

Figure 9. Experimental setup: PPLN is periodically poled lithium niobate (PPLN) crystal; F is a band bass filter at 775 nm; M is mirror; NF is neutral density filter; NPBS1 and NPBS2 are nonpolarizing beam splitters; MO1, MO2, and MO3 are microscope objectives with (50 × , NA = 0.45), (20 × , NA = 0.45), and (20 × , NA = 0.1), respectively.

http://dx.doi.org/10.5772/66082

The off-axis digital hologram recorded by the CCD camera was reconstructed using convolution-based Fresnel method. Three spectra were obtained when 2D-FFT was implemented to the off-axis hologram as shown in **Figure 10**. Only one filtered spectrum from the three spectra in 2D-FFT is used. The inverse 2D-FFT was applied after filtering out the spectrum, and the calculation result gives a complex object wave (amplitude and phase). The obtained complex amplitude was multiplied by the digital reference wave $R_D(m,n)$ to generate the final amplitudes and phases. An amplitude-contrast image and a phase-contrast image can be obtained by using the following intensity $[\mathrm{Re}(\Gamma)^2 + \mathrm{Im}(\Gamma)^2]$ and the argument $\arctan[\mathrm{Re}(\Gamma)/\mathrm{Im}(\Gamma)]$, respectively. The digital reference wave $R_D(m,n)$ can be calculated as $R_D(m,n) = A_R \exp[i(2\pi/\lambda)(k_x m\Delta x + k_y n\Delta y)]$, where A_R is the amplitude, λ is the wavelength of the light source(777.8 nm for the femtosecond pulse light), and k_x and k_y are the two components of the wave vectors, which are adjusted such that the propagation direction of $R_D(m,n)$ matches as closely as possible with that of the experimental reference wave. The reconstructed amplitude and phase were recorded by selecting the appropriate values of the two components of the wave vector $k_x = 0.02145\ \mathrm{mm}^{-1}$ and $k_y = -0.51570\ \mathrm{mm}^{-1}$. In order to see the effectiveness of our method compared to the conventional DHM, the femtosecond pulse light and PPLN crystal were replaced by long coherent He-Ne laser light source ($\lambda = 632.8$ nm).

The obtained off-axis hologram was reconstructed with the same procedure of **Figure 10** and the final amplitude and phase obtained at $k_x = 0.00999\ \mathrm{mm}^{-1}$ and $k_y = -0.5239\ \mathrm{mm}^{-1}$. **Figure 11 (a)** and **(d)** shows the off-axis holograms of the sarcomere sample obtained by a He-Ne laser light and femtosecond pulse light, respectively. A layered structure of around 15 sarcomeres

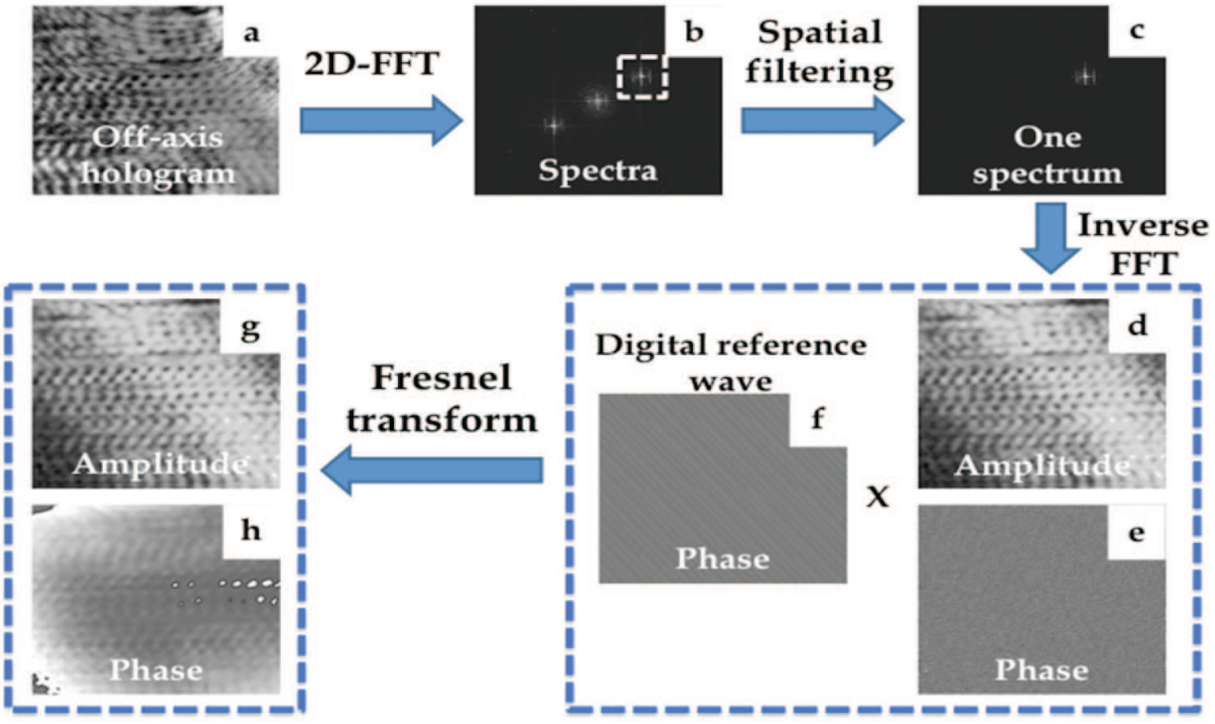

Figure 10. Sequential reconstruction steps (a) off-axis hologram, (b) Fourier transformed spatial frequency domain data, (c) filtered one spectrum, (d) and (e) reconstructed amplitude and phase before removing the fringes in the observation plane, (f) digital reference wave, and (g) and (h) final amplitude and phase maps.

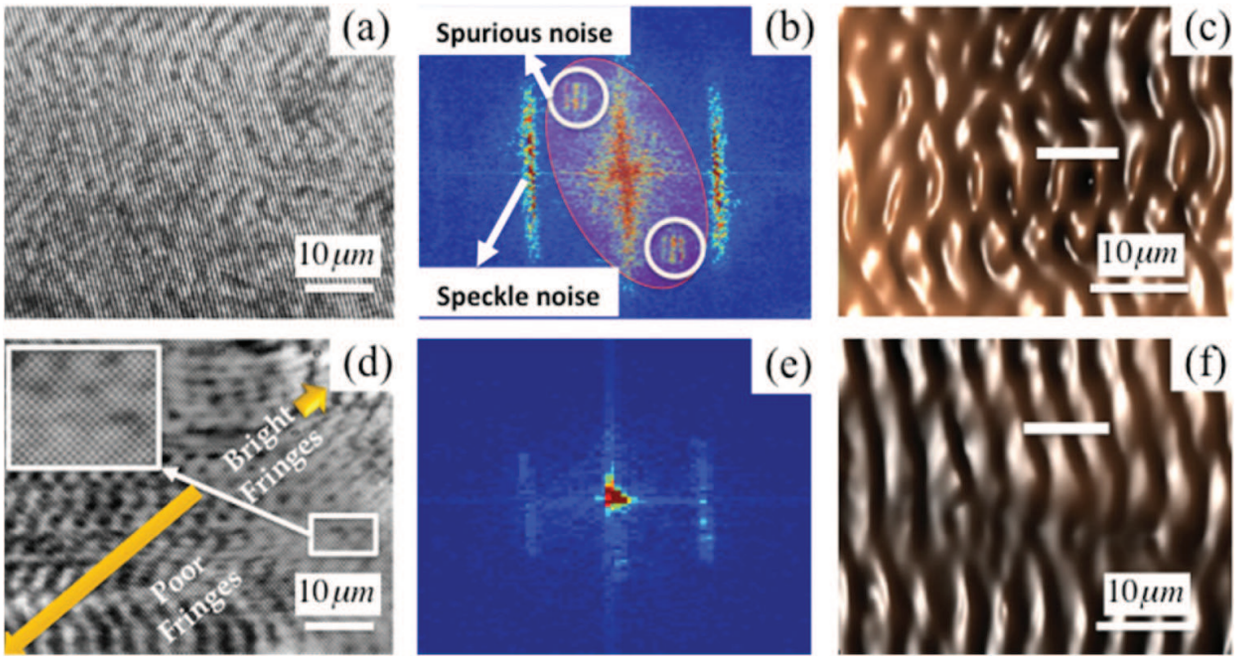

Figure 11. Off-axis holograms of layered structure of sarcomeres taken by (a) He-Ne laser light and (d) femtosecond pulse light. (b) and (e) are filtered 2D-FFT spectrum of (a) and (b), respectively. (c) and (f) are 3D pseudocolor reconstructed phase-contrast image of stripy sarcomere with He-Ne laser light and femtosecond pulse light, respectively.

was captured at nearly same region of FOV. Comparison of these images indicated that the image brightness of DHM with the femtosecond pulse light was higher than that of the He-Ne laser light due to temporally localized energy of the femtosecond pulse light. **Figure 11(b)** and **(e)** shows one filtered spectrum from the three spectra in frequency domain when two-dimensional fast Fourier transform (2D-FFT) has been used for the off-axis interferogram as shown in **Figure 11(a)** and **(d)**, respectively. Note that the three spectra appearing in the filtered one spectrum are due to the off-axis fringes of the sarcomere sample itself. **Figure 11(b)** shows the appearance of both spurious and speckle noises, while such noise was totally disappearing by using our setup as shown in **Figure 11(e)**. In order to see the effectiveness of our setup compared to the conventional DHM with He-Ne laser light, we have not applied any of the numerous image enhancement techniques, to significantly improve the perceived image quality for biological applications. **Figure 11(c)** and **(f)** shows 3D pseudocolor reconstructed phase-contrast images of stripy sarcomere of **Figure 11(a)** and **(d)**, respectively. Although phase images tend to suffer from the coherent noise to a significantly less degree compared to the amplitude images, the sarcomeres are hardly viewed in **Figure 11(c)** because of the existence of coherent noise at the background. In contrast, **Figure 11(f)** shows that the stripe structures of 10 sarcomeres are clearly viewed in the phase-contrast image because of no coherent noise in the background image. The phase profiles extracted along white lines in the phase-contrast image of **Figure 11(c)** and **(f)** are shown in **Figure 12**, indicating the cross-sectional profile of two sarcomeres. As shown from **Figure 12**, the phase profile of the proposed technique (red color) is free from noise, and the sarcomere cross section can be calculated precisely with no need of image enhancement techniques, which in turn takes time to enhance the image to some amount.

The phase profiles have been measured at different locations, and the average phase profile of the proposed method was found to be in good agreement with nominal values of the sarcomere depth. The contrast (axial resolution) of the proposed method is estimated from **Figure 12** to be two times better than the contrast of He-Ne phase-based result. It is noted that the mismatching in the peaks of the phase profiles shown in **Figure 12** is due to difference in magnifications of the captured off-axis holograms of both He-Ne and femtosecond pulse light. To enhance the differentiation of the sarcomere structure within the reconstructed amplitude map, the 3D reconstructed amplitude maps of both He-Ne laser light and femtosecond pulse light may be displayed in a false color representation as shown in **Figure 13(a)** and **(b)**, respectively.

It is noted that these 3D reconstructed amplitude maps were flipped upside down to see the sarcomeres from different views. In **Figure 13(a)**, existence of coherent noise in the background image makes it difficult to visualize the structure of the sarcomeres. On the other hand, **Figure 13(b)** shows the high quality and contrast of structure detail on the sarcomeres and

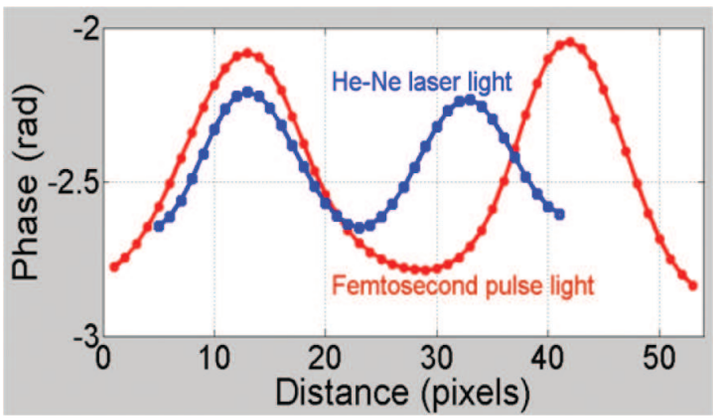

Figure 12. Phase profiles extracted along white lines of two sarcomeres in phase-contrast images of both **Figure 11(c)** (blue color) and **Figure 11(f)** (red color).

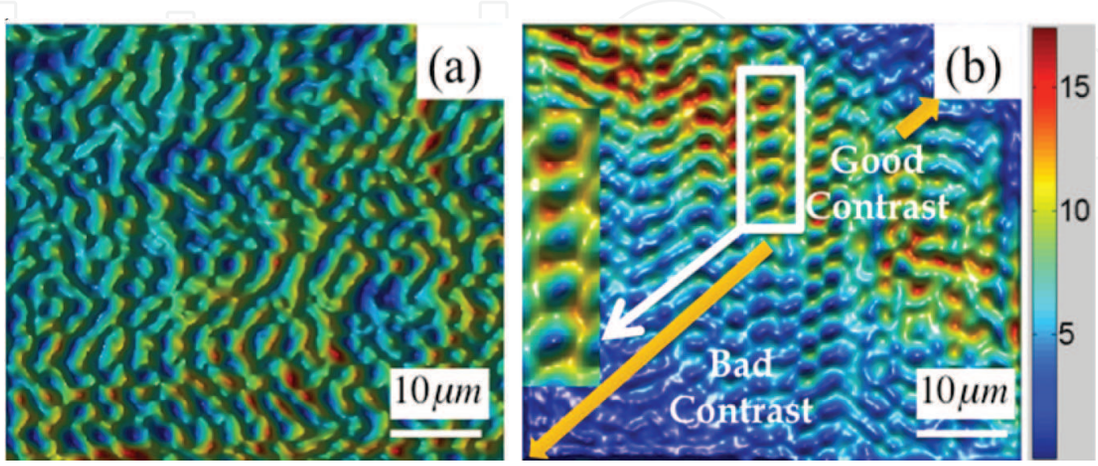

Figure 13. 3D pseudocolor reconstructed amplitude-contrast image of (a) He-Ne laser light and (b) femtosecond pulse light.

provides accurate profile edges of hexagonal shape of the sarcomeres. This makes our technique preferable in featuring such sandwiched biological samples, which is quite difficult to investigate using atomic force microscope (AFM).

Our deductions were verified by applications of apodization technique [10], to estimate the coherent noise level in the reconstructed amplitude maps of the off-axis holograms generated by both He-Ne and femtosecond pulse light, respectively. Apodization is the same topic as windowing in signal processing. The transmission of the apodized aperture function is completely transparent in the large central part of the profile. At the edges, the transmission varies from zero to unity following a curve defined by a cubic spline interpolation. The 2D transmission size of (480 × 480) pixels of the apodized aperture function is multiplied with the off-axis holograms (480 × 480) pixels of both He-Ne laser light and femtosecond pulse light, respectively. Normalization of intensity distribution of four sarcomeres at the middle of the off-axis hologram of the He-Ne laser light before and after application of apodization is shown in the left side of **Figure 14**. Normalization of intensities distribution of four sarcomeres at the middle of the off-axis hologram of the femtosecond laser light before and after application of apodization is shown in the right side of **Figure 14**.

As seen from the left figure, the variation in intensities before and after application of apodization function indicates that there is a coherent noise in the reconstructed amplitude of He-Ne off-axis hologram. Such coherent noise is totally disappearing in the right figure, whereas no variation in intensities before and after application of apodization. This confirms that the reconstructed amplitude of femtosecond pulse light off-axis hologram is free from coherent noise. Due to the short coherence length of the pulsed light, only fraction of hologram shows high-contrast fringe, resulting in a good reconstruction in this region as shown in **Figure 13(b)** which is corresponding to the off-axis hologram of **Figure 11(d)**. The contrast of the fringes in **Figure 11(d)** reduces from center to two sides diagonally, which indicates the zero-path-difference point is nearly in the middle of the sensor. To obtain a high-brightness full-field image, we can move the center of the fringes diagonally and collect holograms with different zero path difference. Twelve off-axis holograms were generated diagonally by varying the optical path length of the interferometer to cover a sarcomere sample of around 45 × 45 micrometers in the field of view (FOV) with high-contrast fringes at different regions in the

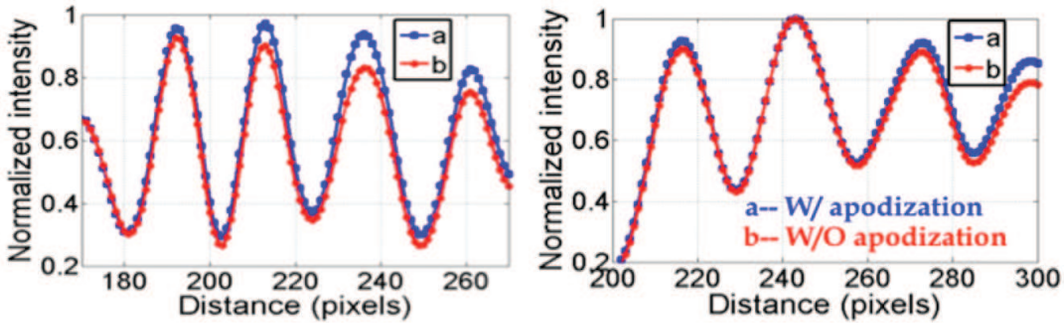

Figure 14. Normalization of intensities distribution of four sarcomeres with (a) and without (b) apodization taken at the middle of the off-axis holograms of He-Ne laser light (left) and femtosecond pulse light (right).

http://dx.doi.org/10.5772/66082

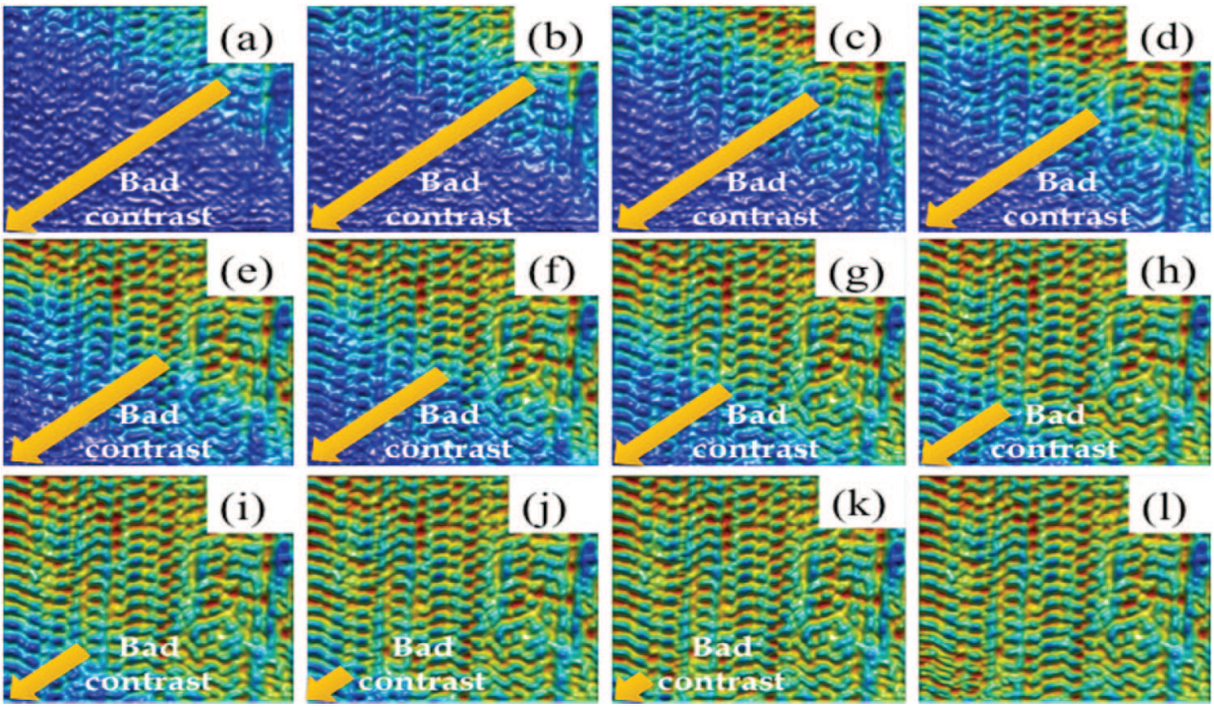

Figure 15. 3D pseudocolor reconstructed amplitude-contrast image from superimposing of (a) 1 hologram, (b) 2 holograms, (c) 3 holograms, (d) 4 holograms, (e) 5 holograms, (f) 6 holograms, (g) 7 holograms, (h) 8 holograms, (i) 9 holograms, (j) 10 holograms, (k) 11 holograms, and (l) 12 holograms produced by femtosecond pulse light by using linear direct method.

image. The full-field image can be obtained by adding multiple such single reconstructions on the intensity basis as shown in **Figure 15(a)–(l)**. The synthesized image map is shown in **Figure 15(l)**. Because of the holograms' shifting process, the reference and object beam will have some phase shifts when the second hologram is recorded. When the second hologram is subtracted from the first hologram, the zero order is removed. Subtractions among successive holograms were superimposed using a direct linear addition method to constitute a full-field, high-quality synthesized hologram as shown in **Figure 9**. The intensity of the synthesized hologram I can be written as follows:

$$I_{synth} = \sum_{i=1}^{N/2} (h_N - h_i) + \sum_{i=1}^{N/2} (h_i - h_N), \tag{22}$$

where i takes from 1 to N, whereas N is the total number of off-axis holograms = *12*.

5. Off-axis terahertz DH using continuous-wave THZ radiation

Terahertz (THz) radiation is an electromagnetic radiation lying between the microwave and infrared portions of the spectrum as shown in **Figure 16**. THz radiation can be produced by many techniques such as quantum cascade lasers (QCLs). QCLs are semiconductor heterostructures that can emit continuous-wave (CW) THz radiation [10]. QCLs are electron-only

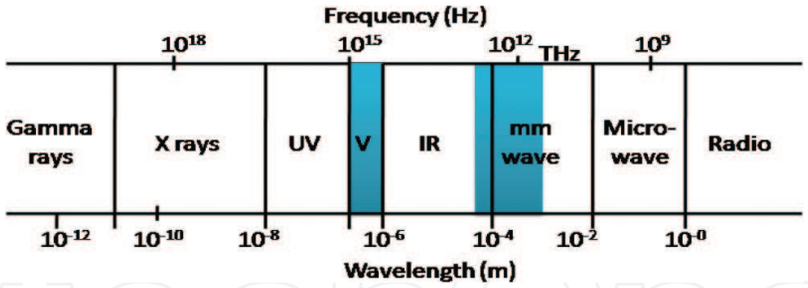

Figure 16. Spectrum of waves showing the location of THz radiation.

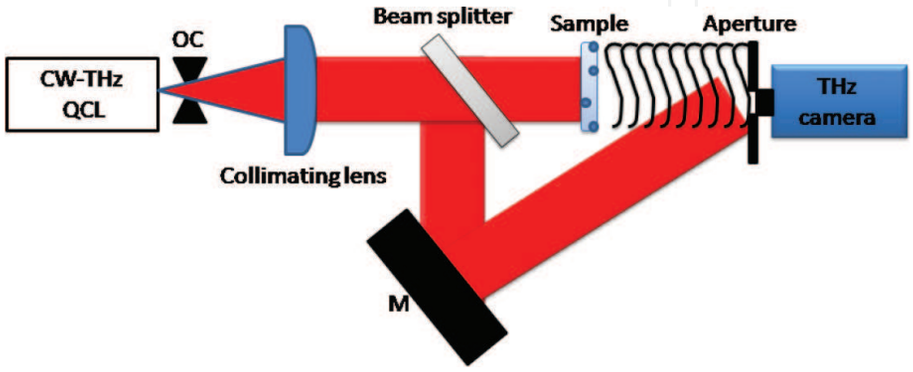

Figure 17. Experimental setup of CW THz-DH: OC is optical chopper and M is a mirror.

devices that exploit transitions between conduction band states. The conduction band offsets between neighboring materials in the superlattice create a series of quantum wells and barriers. The most widely used QCL designs are based on GaAs/AlGaAs superlattices. The word cascading means that one electron can produce many photons in the superlattice periods. A significant advantage of THZ radiation is that it can easily inspect sealed packages for contrasting metal and plastic objects, testing pharmaceutical tablets for integrity, detecting skin cancers, etc.

In Section 5, we present the usage of THz radiation for 3D surface characterization via a digital holography (DH) technique [11]. Since the usual DH uses a visible light, it is difficult to visualize 3D internal structure of visibly opaque objects due to their limited penetration depth. The compelling advantage of THz radiation is that it has a good penetration capability; thus, 3D visualization of both surface shape and internal structure in visibly opaque object can be achieved [12]. We constructed off-axis THz digital holography (THz-DH) system equipped with CW-THz radiation generated by QCL, and the THz digital hologram is captured by a THz camera.

Figure 17 illustrates a schematic diagram of off-axis THz-DH system. An optical chopper (OC) is positioned in front of the QCL to reduce the noise. The radiation was collimated by a Teflon lens (f = 300 mm). The collimated THz beam of diameter around 60 mm is divided into a signal THz beam and a reference one by a silicon beam splitter (BS). **Figure 18(a)** shows 2D intensity distribution of the THz beam without the sample. **Figure 18(b)** shows the dark frame captured

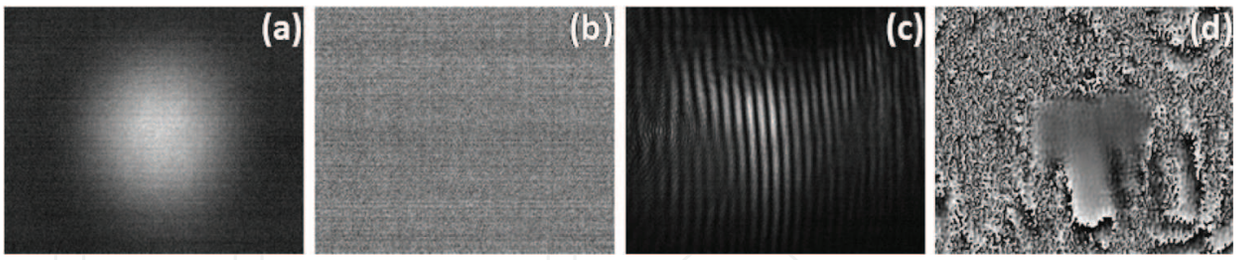

Figure 18. (a) A 2D intensity distribution of the THz beam without the sample, (b) dark frame captured by the THz camera when there is no illumination, (c) off-axis hologram, and (d) 3D phase-contrast image reconstructed by angular spectrum method.

by the THz camera when there is no illumination. The signal THz beam passed through a sample (here, the sample is a letter T from paper), while a reference THz beam is reflected by a mirror (M). Then, these two THz beams were spatially overlapped at a certain off-axis angle to generate 2D fringe of THz beams. Finally, the off-axis THz digital hologram is captured by a THz camera as shown in **Figure 18(c)**. The off-axis THz hologram has been reconstructed with angular spectrum method to extract both amplitude and phase. **Figure 18(d)** shows the 3D reconstructed phase of the sample.

6. Conclusion

In conclusion, we have presented the recent developments of digital holography techniques for surface characterization. In this chapter, the principle of digital holography with focus on numerical reconstruction algorithms is presented. Also, influence of slightly imperfect collimation of the reference wave in off-axis DH is discussed. Finally, we have described two different DH techniques for surface characterization: the first technique by using short coherent length, namely, high-brightness DHM, and the second technique by using long coherent length, namely, THz-DH. Experimental results are presented to verify the principles.

Author details

Dahi Ghareab Abdelsalam[1]*, Takeshi Yasui[2], Takayuki Ogawa[2] and Baoli Yao[3]

*Address all correspondence to: shosho_dahi@yahoo.com

1 Engineering and Surface Metrology Laboratory, National Institute for Standards, Egypt

2 Graduate School of Science and Technology, Tokushima University, Japan

3 State Key Laboratory of Transient Optics and Photonics, Xi'an Institute of Optics and Precision Mechanics, Chinese Academy of Sciences, China

References

[1] Goodman, J.W.; & Lawrence, R.W.: Digital image formation from electronically detected holograms, Applied Physics Letters. 1967; **11**: 77-79.

[2] Schnars, U.; & Juptner, W.: Direct recording of holograms by a CCD target and numerical reconstruction, Applied Optics. 1994; **33**: 179-181.

[3] Juptner, W.; & Schnars, U.: Digital Holography: Digital Hologram Recording, Numerical Reconstruction, and Related Techniques, Springer-Verlag, Berlin. (2005).

[4] Yaroslavsky, L.P.; & Merzlyakov, N.S.: Methods of Digital Holography, Consultants Bureau, New York (1980).

[5] Kreis, T.M.; & Juptner, W.: Principles of digital holography. In Juptner, W. & Osten, W. (Eds.) Fringe '97, Proceeding of 3rd International Workshop on Automatic Processing of Fringe Patterns. Akademie, Berlin. (1997).

[6] Hecht, E.: Optics, Addison Wesley Longman, Inc., San Francisco, United States of America (1998). p. 485.

[7] Kim, M.K.; Yu, L.; & Mann, C.J.: Interference techniques in digital holography. Journal of Optics A: Pure and Applied Optics. 2006; **8**: 518-523.

[8] Abdelsalam, D.; Baek, B.; & Kim, D.: Influence of the collimation of the reference wave in off-axis digital holography. Optik. 2012; **123**: 1469-1473.

[9] Abdelsalam, D.; Yamamoto, H.; & Yasui, T.: High Contrast Digital Holographic Microscopy by use of Femtosecond Pulse light. JSAP-OSA Joint Symposia, paper 15p_2F_3. (2015).

[10] D.G. Abdelsalam, and Daesuk Kim, "Coherent noise suppression in digital holography based on flat fielding with apodized apertures", Optics Express, 19, pp. 17951-17959, (2011).

[11] Takayuki, O.; Abdelsalam, D.; Masuoka, T.; Yasui, T.; & Yamamoto, H.: Off-Axis Terahertz Digital Holography using Continuous-Wave Terahertz radiation. Conference on Lasers and Electro-Optics Pacific Rim, paper 27P_99. (2015).

[12] Li, Q.; Xue, K.; Li, Y.-D.; & Wang, Q.: Experimental research on terahertz Gabor inline digital holography of concealed objects. Applied Optics. 2012; **51**, 7052-7058.